Acta Geochim (2024) 43:838–855
https://doi.org/10.1007/s11631-024-00673-7

ORIGINAL ARTICLE

Petrology, geochemistry, and crystal size distribution of the basaltic andesite–dacite association at Mt. Sumbing, Central Java, Indonesia: Insights to magma reservoir dynamics and petrogenesis

Indranova Suhendro[1,2] · Endra Yuliawan[1] · Revina Fitri Zen[1] · Zulfa Yogi Rahmawati[1] · Pandu Eka Priyana[1] · Sonna Diwijaya[1] · Muhammad Alsamtu Tita Sabila Pratama Suhartono[1] · Andre Jonathan[1] · Gammanda Adhny El Zamzamy Latief[1]

Received: 21 September 2023 / Revised: 13 December 2023 / Accepted: 5 January 2024 / Published online: 23 February 2024

Abstract Ten rock samples consisting of one pyroclastic density current (PDC1) deposit, seven lava flows (LF1–7), and two summit lava domes (LD1, 2) were studied to understand the petrogenesis and magma dynamics at Mt. Sumbing. The stratigraphy is arranged as LF1, PDC1, LF2, LF3, LF4, LF5, LF6, LF7, LD1, and LD2; furthermore, these rocks were divided into two types. Type I, observed in the oldest (LF1) sample, has poor MgO and high Ba/Nb, Th/Yb and Sr. The remaining samples (PDC1–LD2) represent type II, characterized by high MgO and low Ba/Nb, Th/Yb and Sr values. We suggest that type I is derived from AOC (altered oceanic crust)-rich melts that underwent significant crustal assimilation, while type II originates from mantle-rich melts with less significant crustal assimilation. The early stage of type II magma (PDC1–LF3) was considered a closed system, evolving basaltic andesite into andesite (55.0–60.2 wt% SiO_2) with a progressively increasing phenocryst (0.30–0.48 ϕ_{PC}) and decreasing crystal size distribution (CSD) slope (from − 3.9 to − 2.9). The evidence of fluctuating silica and phenocryst contents (between 55.9–59.7 wt% and 0.25–0.41 ϕ_{PC}, respectively), coupled with the kinked and steep (from − 5.0 to − 3.3) CSD curves imply the interchanging condition between open (i.e., magma mixing) and closed magmatic systems during the middle stage (LF4–LF6). Finally, it underwent to closed system again during the final stage (LF7–LD2) because the magma reached dacitic composition (at most 68.9 wt% SiO_2) with abundant phenocryst (0.38–0.45 ϕ_{PC}) and gentle CSD slope (from − 4.1 to − 1.2).

Keywords Sumbing · Whole-rock geochemistry · Petrogenesis · Fractionation · Magma mixing · Crystal size distribution

1 Introduction

The Central Java volcanic field (herein referred to as CJVF; covering the area of Central Java and Yogyakarta provinces) has been considered as one of the densest volcanic regions in Indonesia. In particular, there are seven major active stratovolcanoes incorporated within the CJVF, including Merapi, Merbabu, Lawu, Sindoro, Sumbing, Slamet, and Ungaran (Fig. 1a). Noteworthy, these volcanoes are located adjacent to the popular tourist towns (e.g., Yogyakarta, Wonosobo, Semarang, and Banyumas), with population density ranging from 492 to 12 232 people/km^2 (Badan Pusat Statistik 2020). Previous studies have shown that some of the aforementioned volcanoes are capable of producing VEI 4 eruptions, which have been large enough to cause significant disruption to human living (e.g., Gertisser et al. 2012; Surono et al. 2012; Prambada et al. 2016; Harijoko et al. 2021). Among the aforementioned CJVF volcanoes, Mt. Sumbing is considered the least studied one because the geological data is still lacking (i.e., stratigraphy, eruption age, geochemistry, and textural studies). Dempsey (2013) has shown the geochemical variations of Sumbing rocks (i.e., whole-rock and plagioclase compositions, and isotope study); however, his samples are limited to the lower flank deposits (below 1600 m.a.s.l). This may indicate that Dempsey (2013) studied relatively old products; hence, our knowledge of the younger/recent products remains lacking.

✉ Indranova Suhendro
indranova.suhendro@ugm.ac.id

[1] Department of Environmental Geography, Faculty of Geography, Universitas Gadjah Mada, Sekip Utara Jl. Kaliurang, Bulaksumur, Yogyakarta 55281, Indonesia

[2] Centre for Disaster Studies, Universitas Gadjah Mada, Jl. Mahoni C-16, Bulaksumur, Yogyakarta 55281, Indonesia

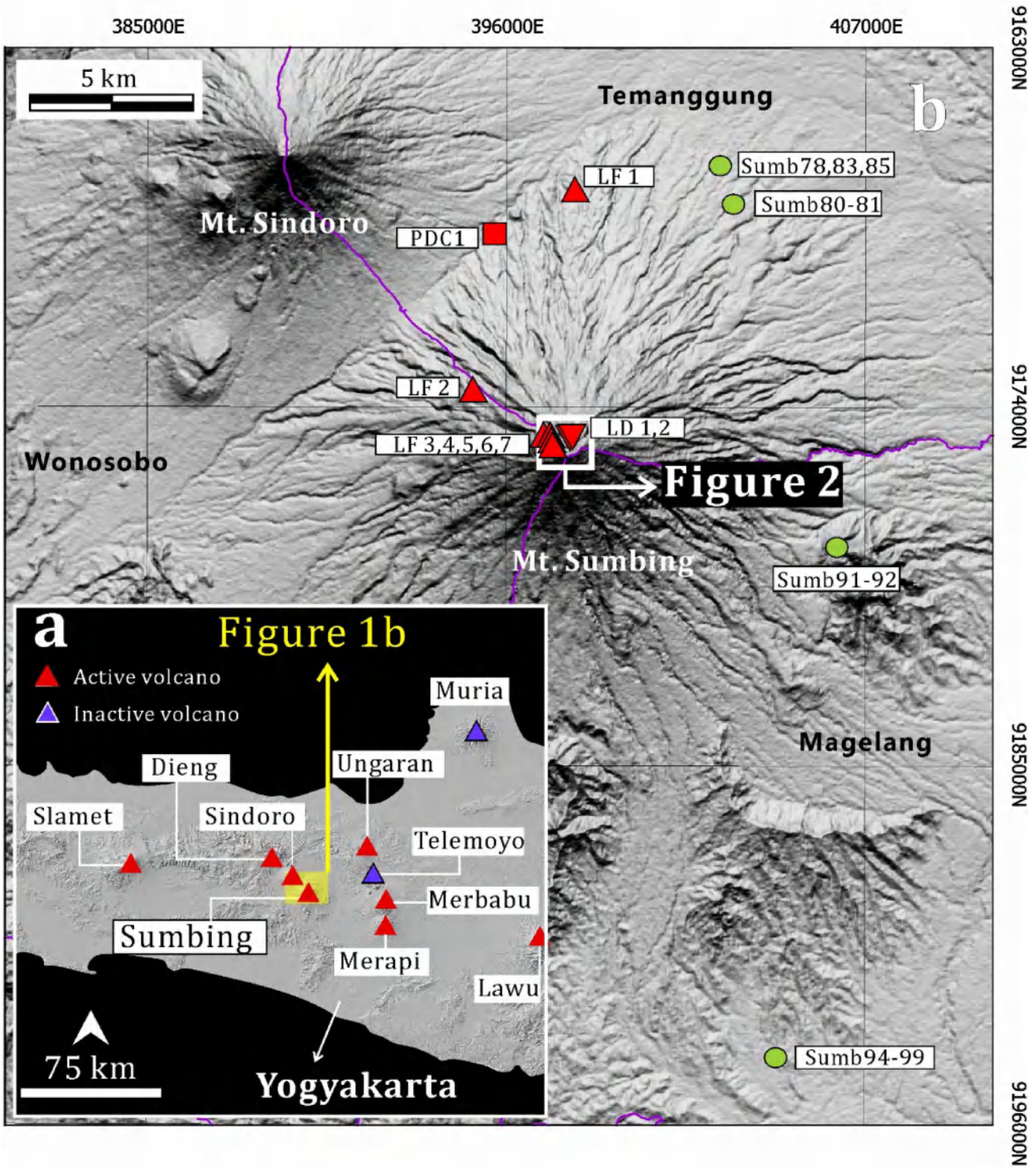

Fig. 1 **a** Distribution of stratovolcanoes in Central Java, Indonesia. The location of Mt. Sumbing is highlighted by yellow square. Red and blue triangles in **a** represent active and inactive volcanoes, respectively. **b** Sampling locations of this study and previous study (i.e., Dempsey 2013). LF, LD, and PDC denotes lava flow, lava dome, and pyroclastic density current, respectively. While Sumb notation represents the original sample code from Dempsey (2013), including lava flow and/or pyroclastic samples. Digital elevation model (DEM) was obtained from Badan Informasi Geospasial 2018 (Open source)

To reduce such a gap, we studied the relatively younger rocks at Mt. Sumbing, covering the flank and summit-crater of the northern regions (from 1120 to 3371 m.a.s.l; Fig. 1b). Fieldwork data was coupled with satellite image analysis to define the temporal relationship (i.e., stratigraphy) between each collected sample, where the summit lava domes are representing the youngest eruptive product (erupted in 1730 CE; Taverne 1926). Subsequently, we conducted petrography, whole-rock geochemistry, and crystal size distribution (CSD) studies to investigate the petrogenesis and dynamics of the present magmatic system beneath Mt. Sumbing. Petrology, geochemistry, and CSD results suggest the occurrence of more than one magma reservoir, and magmatic differentiation is strongly controlled by magma conditions (i.e., open or closed systems). Under an open system, the magma received an influx of a hotter-less evolved melt, yielding steep-kinked CSD curves and prohibiting magma from reaching silicic magma composition such as dacite (at most andesite). On the other hand, a closed magmatic system allows the magma to yield linear CSD curves and evolve to dacite composition.

2 Overview of Mt. Sumbing

Mt. Sumbing is an active stratovolcano that lies on a ~35 km-thick Java crust, formed by the subduction zone between the Indo-Australian and Eurasian plates (Tregoning et al. 1994; Wölbern and Rümpker 2016; Wibowo et al. 2022). Using seismic tomography modeling, Bohm et al. (2013) suggest that the magma reservoirs of Mt. Sumbing, Sindoro, and Dieng are located between 15–35 km crustal depth. The published 1:100 000 and 1:50 000 geological maps (Sitorus et al. 1994) show that Mt. Sumbing predominantly consists of lava flows and lacks pyroclastic deposits. However, a recent study by Dempsey (2013) has shown that Mt. Sumbing produces substantial pyroclastic deposits in the form of scoria falls, and scoria-bearing and block and ash pyroclastic density currents (PDCs). Additionally, the present crater of Mt. Sumbing is characterized by the horseshoe-shaped morphology; this crater is filled by the prominent lava domes that erupted in 1730 CE (Taverne 1926). The whole-rock compositions of lava flows and pyroclastic products vary from basaltic andesite to andesite compositions (53–62 wt% SiO_2; Dempsey 2013). Sitorus et al. (1994) also reported the presence of basaltic lithic clasts in the oldest PDC deposits (named Sap. 1); however, this definition is only determined based on the petrographic observation without any geochemistry analyses. Moreover, it is also important to mention (again) that the reported geochemical data by Dempsey (2013) lacked the composition of the summit lava flows and the 1730 CE lava domes (Fig. 1b).

3 Methods

3.1 Fieldwork

Fieldwork was conducted for sampling purposes and to record the structures and/or textures in the observed outcrops. We focus on the northern flank because it provides the most affordable track to reach the summit (i.e., hiking). Numerous outcrops were observed alongside the tracking route; however, samples were collected only from accessible positions, with safety procedures as the primary consideration. Ten observation locations (LOCs) were established, covering one pyroclastic density current (PDC) deposit, seven lava flows, and two summit lava domes (Figs. 1b, 2). Each location is represented by one juvenile sample, and all samples display fresh conditions. Subsequently, the sample from each location is used for laboratory analyses, such as petrography, whole-rock geochemistry (XRF), and crystal size distribution.

3.2 Petrography and crystal size distribution (CSD)

All phenocryst phases were manually digitized using graphic design software (e.g., Corel Draw, Adobe Illustrator) and subsequently processed by Image-J software (open access) to obtain the number and size of the phenocrysts. Furthermore, the obtained number and phenocryst size data were used to quantify average phenocryst diameter ($\overline{d}$), and phenocrystallinity (ϕ_{PC}; vesicle-free) and mineral assemblages as below:

$$\overline{d} = \sum_{n=1}^{N} d_n / N \tag{1}$$

$$\phi_{PC} = \sum_{n=1}^{N} Ac \Big/ \left(A_t - \sum_{n=1}^{N} Av \right) \tag{2}$$

where $\sum_{n=1}^{N} d_n$ is the summation of crystal diameter d_n in mm, N is the number of analyzed crystals in each thin section, $\sum_{n=1}^{N} Ac$ is the summation of the crystal area Ac, $\sum_{n=1}^{N} Av$ is the summation of the vesicle area Av (a parameter that provides the bulk vesicularity), and A_t is the area of the sample.

The digitized plagioclase crystals were selected for CSD analysis because they occur in all samples and are considered the most abundant mineral phase. The crystal aspect ratio (one of the input parameters in the CSD analysis) was determined using CSD *slice* by Morgan and Jerram (2006). Subsequently, the digitized plagioclase crystals were processed by CSD-corrections software to obtain the size distribution, goodness of fit, and regression slope data.

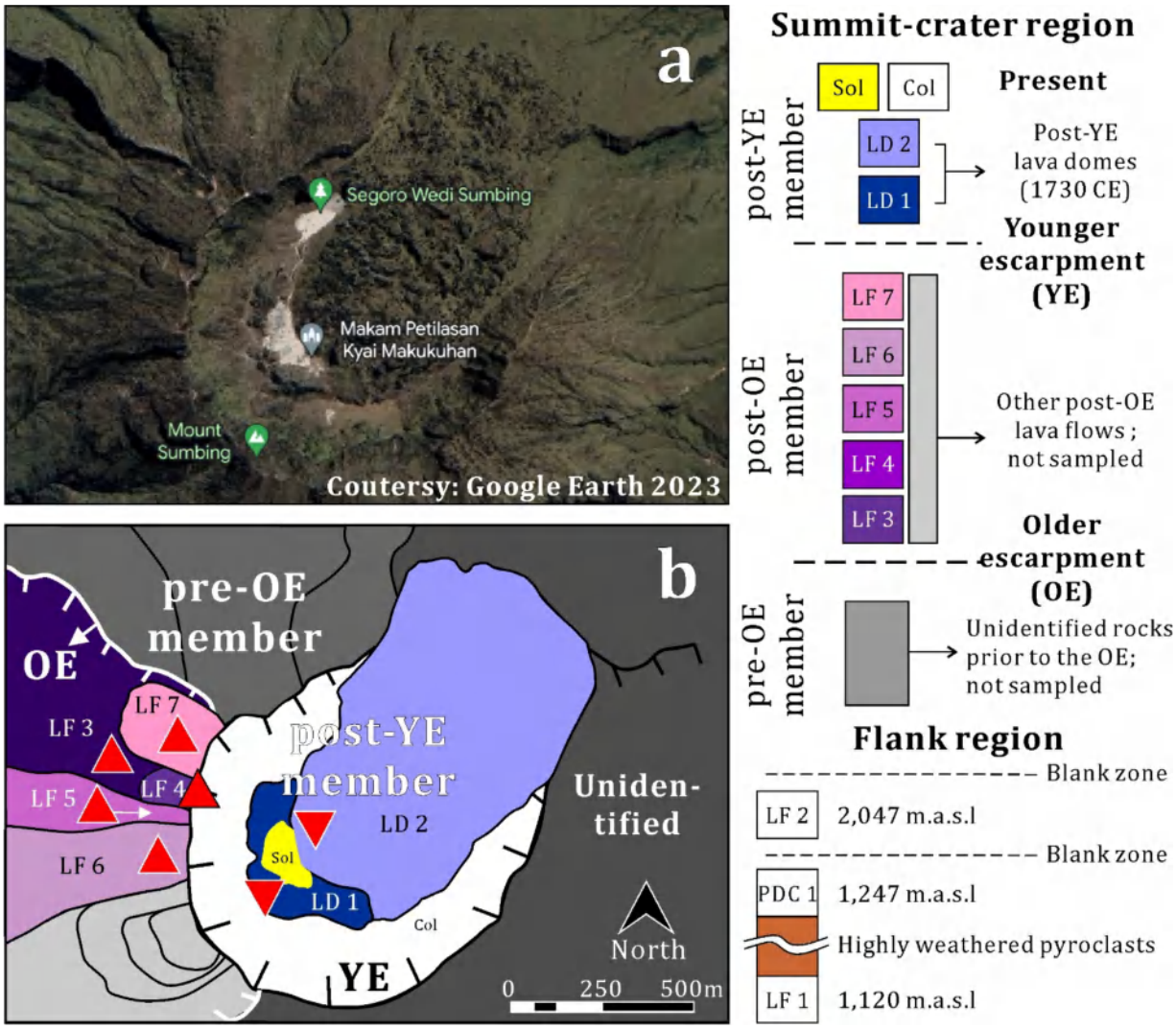

Fig. 2 **a** Satellite image of the summit-crater region of Mt. Sumbing (captured from Google Earth 2023). **b** Simplified rock units of the summit-crater region. The boundary for each unit was determined from fieldwork and qualitative-morphometry observation using satellite image. Note the occurrence of two escarpments, i.e., older (OE) and younger (YE) escarpment. Normal and reversed triangles represent sampling location of the lava flows and lava domes, respectively

3.3 Whole-rock XRF and estimated silica content in the melt

Whole-rock composition of the juvenile product (from each location) was obtained using a WD XRF Axios Max (PANalytical) at the Balai Penyelidikan dan Pengegmbangan Teknologi Kebencanaan Geologi (BPPTKG) Yogyakarta, Indonesia. First, samples were powdered using a ball-milling machine. Second, samples were pressed using a briquet press machine to form pellets (consisting of at least 5 g of powder). Finally, samples were analyzed to determine their major (SiO_2, TiO_2, Al_2O_3, MnO, Fe_2O_3, MgO, CaO, Na_2O, K_2O, and P_2O_5) and trace element (e.g., Ba, Sr, Th, U, Zr, Hf, Nb, Nd, Cr, Sc) compositions.

3.4 Estimated silica content in the melt, temperature, and viscosity

The silica content in the melt (SiO_2^{Melt}) is estimated by subtracting the phenocryst with the bulk-rock composition data based on the following equation (e.g., Mitsuoka et al. 2021):

$$SiO_2^{Melt} = SiO_2^{Bulk} - \sum_i \left(SiO_2^{Phenocryst} \times \phi_{PC} \right) \quad (3)$$

where i represents the phenocryst phases and ϕ_{PC} is the vesicle-free pheno-crystallinity obtained from Eq. 2.

Some studies have shown that silica is inversely proportional to temperature and directly proportional to melt viscosity and magma viscosity (e.g., McBirney and Murase

1984; Murase et al. 1985; Toramaru 2006; Ridolfi and Renzulli 2012; Takeuchi 2015). Therefore, it is possible to roughly estimate these aforementioned parameters using the following equations:

$$T = 1000/[0.16 + \left(0.01 \times SiO_2^{Melt}\right] \quad (4)$$

$$log\mu = \left(0.146 \times SiO_2^{Melt}\right) - 6.3 \quad (5)$$

$$log\mu_{eff} = log\mu + \left[0.019 \times \overline{d} \Big/ \left[\left(\frac{1}{\phi_{PC}}\right)^{1/3} - 1.5\right]\right] \quad (6)$$

where T is the magma temperature in Kelvin (K), $log\mu$ is the melt viscosity (phenocryst-free) in Pa s, and $log\mu_{eff}$ is the magma viscosity (phenocryst-bearing) in Pa s.

4 Results

4.1 Temporal variation of the rock units

Ten rock samples consisting of one pyroclastic density current deposit (PDC1), seven lava flows (LF1–7), and two summit lava domes (LD1 and LD2) were observed during fieldwork (Figs. 1b, 2). The numbering for each sample corresponds to the relative age, where a larger number represents a younger age and vice versa. We determined the relative age (i.e., stratigraphy) of each sample by coupling satellite images (i.e., using the principle of cross-cutting relationship, where younger products cut the older ones) and fieldwork data. Outcrops on the flank region (lower altitudes; 1120–2047 m) comprise three of the oldest eruptive phases (LF1, PDC1, and LF2), while the summit-crater region (higher altitudes; 3201–3371 m) comprise younger eruptive phases, including LF3, LF4, LF5, LF6, LF7, LD1, and LD2.

4.1.1 Flank region (1120–2047 m; LF1, PDC1, and LF2)

LF1 corresponds to the oldest unit because it is located at the lowermost elevation (~1120 m) with dense forest conditions (Fig. 3a). It was a ~5 m thick grey-porphyritic lava flow, which showed no occurrence of vesicles (dense) and structures (massive). This unit is covered by a >15 m thick sequence of highly weathered pyroclastic deposits, as indicated by the red deposit colour (Fig. 3a, b). However, we could not observe the upper portion of the weathered pyroclastic deposits because it is situated on a very steep and inaccessible cliff. Going upward (~1247 m elevation), we observed a ~3 m thick block and ash pyroclastic density current deposit that included scoria as the main juvenile phase (hereafter termed as PDC1) (Fig. 3c). Unlike the highly weathered pyroclastic deposits found above LF1, PDC1 displayed a relatively fresh condition, thus supporting the idea that PDC1 is younger than LF1. LF2 is located at ~2047 m elevation (under dense forest conditions) and corresponds to a >5 m thick grey-porphyritic lava flow (Fig. 3d). In addition, LF2 displayed a massive structure with no occurrence of vesicles. This characteristic is almost identical to the previous lava unit; however, LF2 shows relatively less crystalline condition (i.e., lower phenocryst content) and more ubiquitous pyroxene than that of LF1.

4.1.2 Summit-crater region (3201–3371 m; LF3, LF4, LF5, LF6, LF7, LD1, and LD2)

It is important to mention that outcrop surfaces in the summit-crater region were clearly exposed because of the minimum influence from vegetation. This condition allows us to observe the lava structures clearly and distinguish the boundary between each lava unit, which is important for constructing the stratigraphy (Figs. 2, 3e, f). Notably, all summit-crater region lava flows (LF4–7) are grey in color and porphyritic, have no vesicle textures, and display the following structure: the inner part was typically massive and lacked fractures, while the outer part (which is closer to the ground and surface) was highly fractured and blocky-shaped. A horseshoe-shaped lineament cut these lava flows and presently acts as the rim of the crater morphology (Figs. 2, 3g). Now, two prominent lava domes are present inside the crater, namely LD1 and LD2 (Fig. 3g). Both lava domes are typically white, porphyritic, blocky, and vesicular; however, LD1 is smaller than LD2 (~40 and 100 m thick, respectively). Moreover, LD1 and LD2 are presently cut by an active solfatara-fumarole crater named "Segoro Wedi", which means a sea of sand (Figs. 2, 3h). Representative images of lava flow and lava dome samples are presented in Fig. 3i and j.

4.2 Petrography of Sumbing rocks

Pheno-crystallinity of scoria, lava flows, and lava domes reached 0.30, 0.25–0.48 (avg. of 0.37), and 0.41–0.45 (avg. of 0.43), respectively, with plagioclase (Pl), pyroxene (Px), amphibole (Amp), and oxides (Ox) present as the main phenocryst phases (Fig. 4a). Most of the phenocrysts appear as euhedral crystals; however, some subhedral to anhedral crystal shapes are also present. Among these aforementioned minerals, pyroxene and amphibole occur as two of the most important phases because (1) they resulted in negative correlation, and (2) their abundance varies between each rock type (i.e., scoria, lava flow, and lava dome) (Fig. 4b, c). Both scoria (PDC1) and lava flows (LF1–7) are pyroxene-rich and amphibole-poor; however, scoria had higher pyroxene and lower amphibole fractions

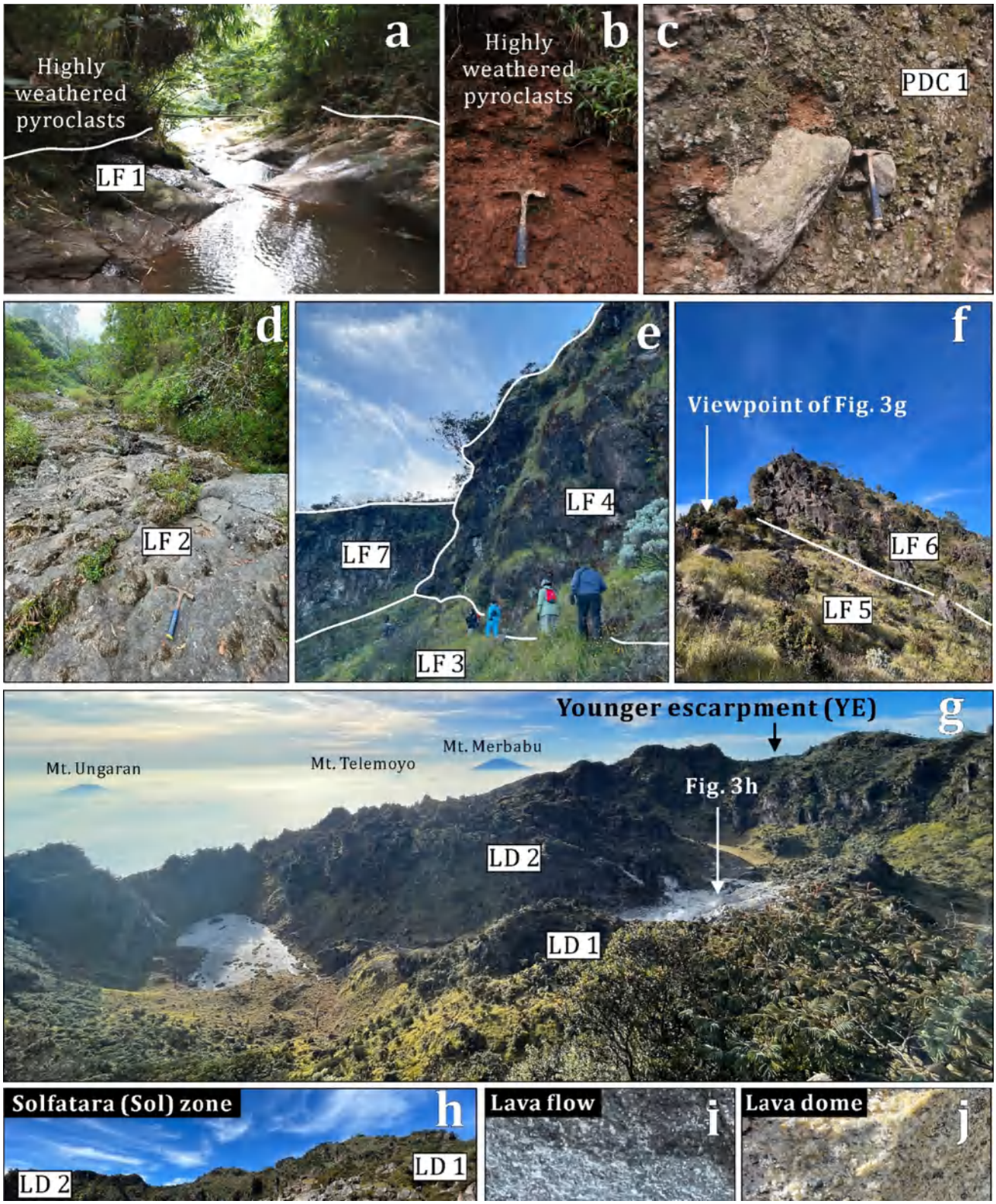

than lava flow samples. In particular, the modal abundance of pyroxene and amphibole phenocrysts reached 29.7 and 0.9 vol% for scoria, and 8.8–25.5 and 2.0–7.8 vol% for lava flows, respectively (Fig. 4c). On the other hand, lava domes showed lower pyroxene and significantly higher amphibole contents, namely 3.2–4.4 and 25.0–29.6 vol%, respectively (Fig. 4c). Unlike pyroxene and oxides (which are characteristically un-zoned), some important textures were observed

◂**Fig. 3** **a** Outcrop image showing the presence of LF1 and highly weathered pyroclastic deposits at 1120 m.a.s.l. **b** Detailed image of highly weathered pyroclastic deposits. **c** Going upward (~127 m difference; 1247 m.a.s.l), we observed a slightly weathered pyroclastic density current deposits that includes scoria as the main juvenile phase. **d** Outcrop image of LF2 at 2047 m.a.s.l. **e**, **f** Fieldwork evidence showing direct contacts between each lava flow in the summit. **g** Morphology of two prominent lava domes (LD1 and LD2) and active solfatara crater at Mt. Sumbing. **h** Closed up image of the solfatara crater, namely Segara Wedi. **i**, **j** Detailed image of the representative lava flow and lava dome samples. Note that lava flow displayed a relatively darker colour and smaller crystal size compared to the lava dome. The hammer is 30 cm in length

in plagioclase and amphibole phenocrysts, such as finely sieved, oscillatory zoned, and ophacitic textures (Fig. 5). In particular, finely sieved texture plagioclases were abundant in LF4 and LF6 samples, and the oscillatory-zoned texture plagioclases are prominent in lava dome samples (LD1 and LD2). While amphiboles display ophacitic texture, except the scoria-PDC1 sample. Additionally, plagioclase and oxide inclusions were commonly observed in amphibole and pyroxene phenocrysts (Fig. 5). It is also important to note that lava dome samples show a relatively larger average phenocryst diameter (0.23–0.25 mm) than those of lava flows (0.18–0.25 mm) and scoria (0.21 mm). Detailed petrographic results are shown in Table 1.

4.3 Geochemistry and physio-chemical properties of Mt. Sumbing's magma

The affinity of our rock samples (shown as $K_2O + Na_2O$ values) falls within a similar range to those of Dempsey (2013) but with typically broader silica contents (from basaltic andesite to dacite; 55.0–68.9 wt% SiO_2) due to the additional analyses of lava dome samples (Fig. 6a). Such composition of Mt. Sumbing lava domes is therefore representing the most silicic Quaternary volcanic rocks within the CJVF (Fig. 5a). Two geochemical patterns were recognized from major (MgO) and trace elements (mobile and immobile; Sr, Ba, Nd, Nb, Th, and Yb) (Fig. 6b–d). The first pattern corresponds to a sample with low MgO and high Ba/Nb–Th/Yb–Sr values, while the second pattern represents samples with high MgO and low Ba/Nb–Th/Yb–Sr values. Hereafter, the first and second geochemical patterns are named types I and II, respectively; type I is exclusive to the oldest unit (LF1), while type II is observed in the remaining units (PDC1 to LD2). Furthermore, both types are characterized by the enrichment of Th and low Zr and Nb anomalies (Fig. 6e). In addition, the primitive mantle-normalized rare earth element (REE) patterns of type I show less enrichment in light REEs and less depletion in heavy REEs than type II (Fig. 6f). It is important to mention that such grouping hypothesis (type I and II) is also observed in Dempsey's samples (Fig. 6b–g). Note that the spiderdiagram of our type II sample exhibits wider variation than that of Dempsey (2013) due to the presence of lava dome samples.

Finally, the estimated silica content in the melt ranges from andesite to rhyolite (58.9–77.1 wt%), with a strong dependence on the crystallization index (i.e., higher phenocrystallinity yields higher silica content in the melt and vice versa) (Fig. 7a–b). As a result, the viscosity ($log\mu$ and $log\mu_{eff}$) of andesitic melts is typically lower than those of dacitic and rhyolitic melts ($10^{2.3–2.6}$ and $10^{3.6–4.7}$, $10^{3.3–3.8}$ and $10^{4.9–5.3}$, $10^{4.4–4.9}$ and $10^{6.4–7.5}$, respectively) (Fig. 7c). In addition, among these melt compositions, andesite yielded the highest temperature (1333–1297 K), followed by dacite (1217–1167 K) and rhyolite (1116–1073 K) (Table 3).

4.4 Plagioclase size distribution of Sumbing rocks

Basaltic andesite and andesite rocks typically have steeper CSD slopes ($-1/Gt$) than those of dacites; namely 3.9, 5.0–2.9, and 1.7–1.2, respectively (Fig. 8). Noteworthy, CSD slope showed a negative correlation with silica, and silica is positively correlated with pheno-crystallinity and average phenocryst size (Fig. 8). We identified that the CSD slope of type II initially decreased from PDC1 to LF3, and subsequently fluctuated from LF4 to LF6 (Table 1). Finally, the CSD slope progressively decreased again from LF7 to LD2 (Table 1). It is also important to note that we cannot identify the temporal variation of the CSD slope for the type I magma because the data is lacking (only one sample; LF1).

5 Discussion

5.1 Petrogenesis of Mt. Sumbing's magma reservoirs and their relationship with Mt. Sindoro

Many studies have shown that a similar magmatic origin is characterized by the linear correlation (i.e., single trend) of major and trace element compositions (e.g., Ginibre et al. 2004; Kaneko et al. 2007; Forni et al. 2016). Therefore, the fact that Mt. Sumbing rocks displayed two distinct trends in MgO, Ba/Nb, Th/Yb, and Sr contents strongly suggests that there are (at least) two magma reservoirs beneath Mt. Sumbing (Figs. 9, 10), where each magma type experienced different crystallization/differentiation histories.

In general, barium (Ba) is abundant in slab components due to its high mobility in fluids and melts, thorium (Th) is typically fluid-immobile and abundant in oceanic sediments, while niobium (Nb) is abundant in the mantle as it is considerably immobile. This is the reason why the ratios of Ba to Nb [as well as the ratios of Th to LREEs, such as ytterbium (Yb) and/or neodymium (Nd)] are generally used to determine the extent of mantle influx and altered oceanic crust component during magma evolution (e.g., Davidson

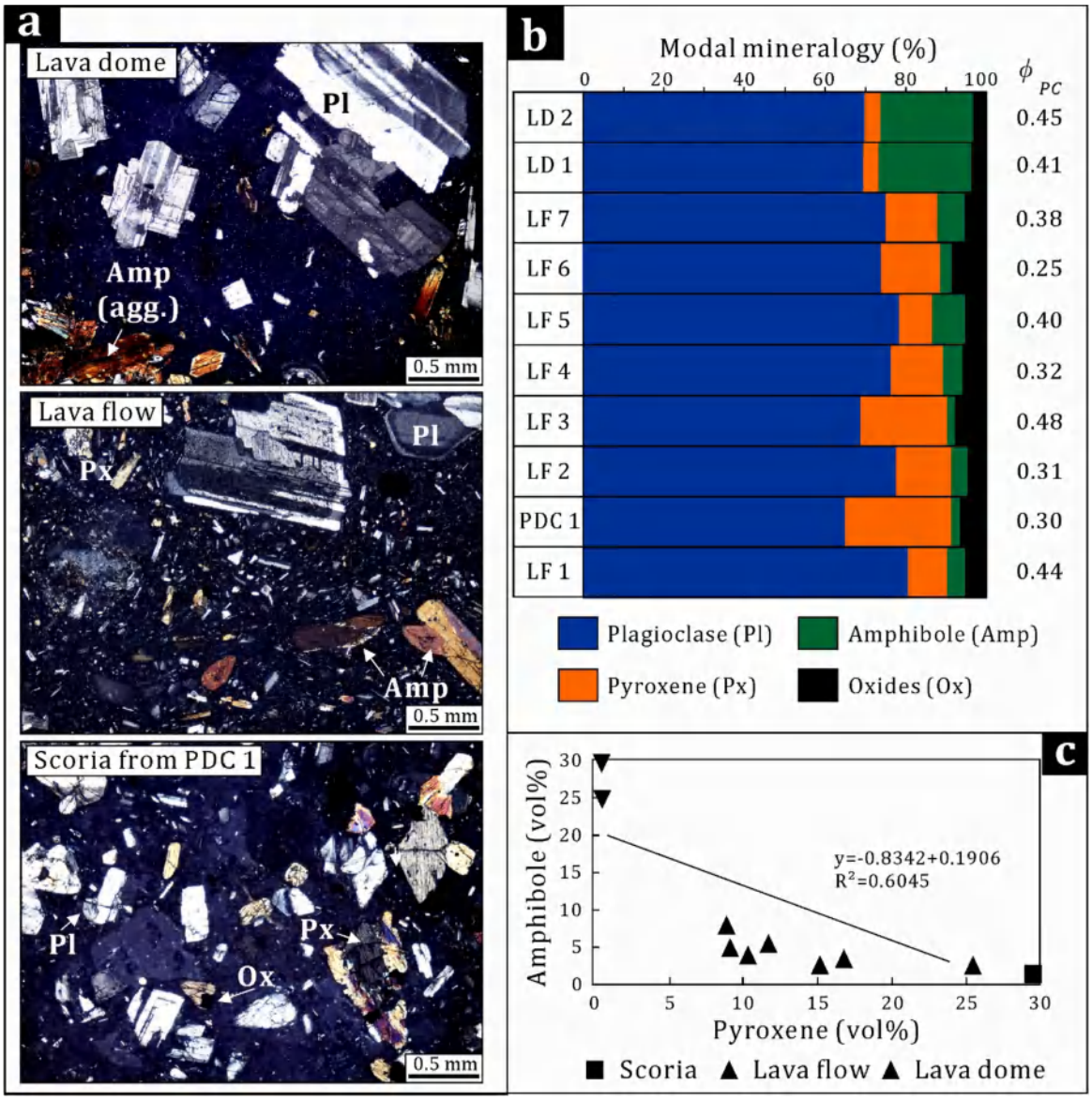

Fig. 4 **a** Representative photomicrograph of lava dome, lava flow, and scoria samples. **b** Modal mineralogy and phenocryst fraction according to the stratigraphic order. Note that lava flows and scoria samples are typically rich in pyroxene, while lava domes are rich in amphibole. **c** This evidence is confirmed by the negative correlation between amphibole and pyroxene

1987; Elliot et al. 1997; De Astis et al. 2000; Münker et al. 2004; Pearce et al. 2005; Straub et al. 2020; Wibowo et al. 2022). The evidence that type I magma has typically high Ba/Nb, Ba/Yb, and Th/Yb ratios with low magnesium values suggests a low mantle influx with a high AOC component; conversely, type II magma received a high mantle influx with less significant AOC component due to the low Ba/Nb, Ba/Yb, and Th/Yb ratios and high magnesium values (Fig. 8). The strontium (Sr) value is often used as a proxy to determine the extent of crustal contamination, where a higher Sr value represents a larger input of crustal material and vice versa (e.g., Handley 2007). Thus, it is likely that type I magma experienced a more significant assimilation process during magma differentiation than type II magma because of the significantly higher Sr values (Fig. 8).

To be fair, it is important to address that the studied sample of Mt. Sumbing (both from this study and Dempsey (2013)) lacks a mafic end member (i.e., basalt; Fig. 6a, b); hence, there is a possibility that the magma derived from the partial melting of the crust. However, the fact that both

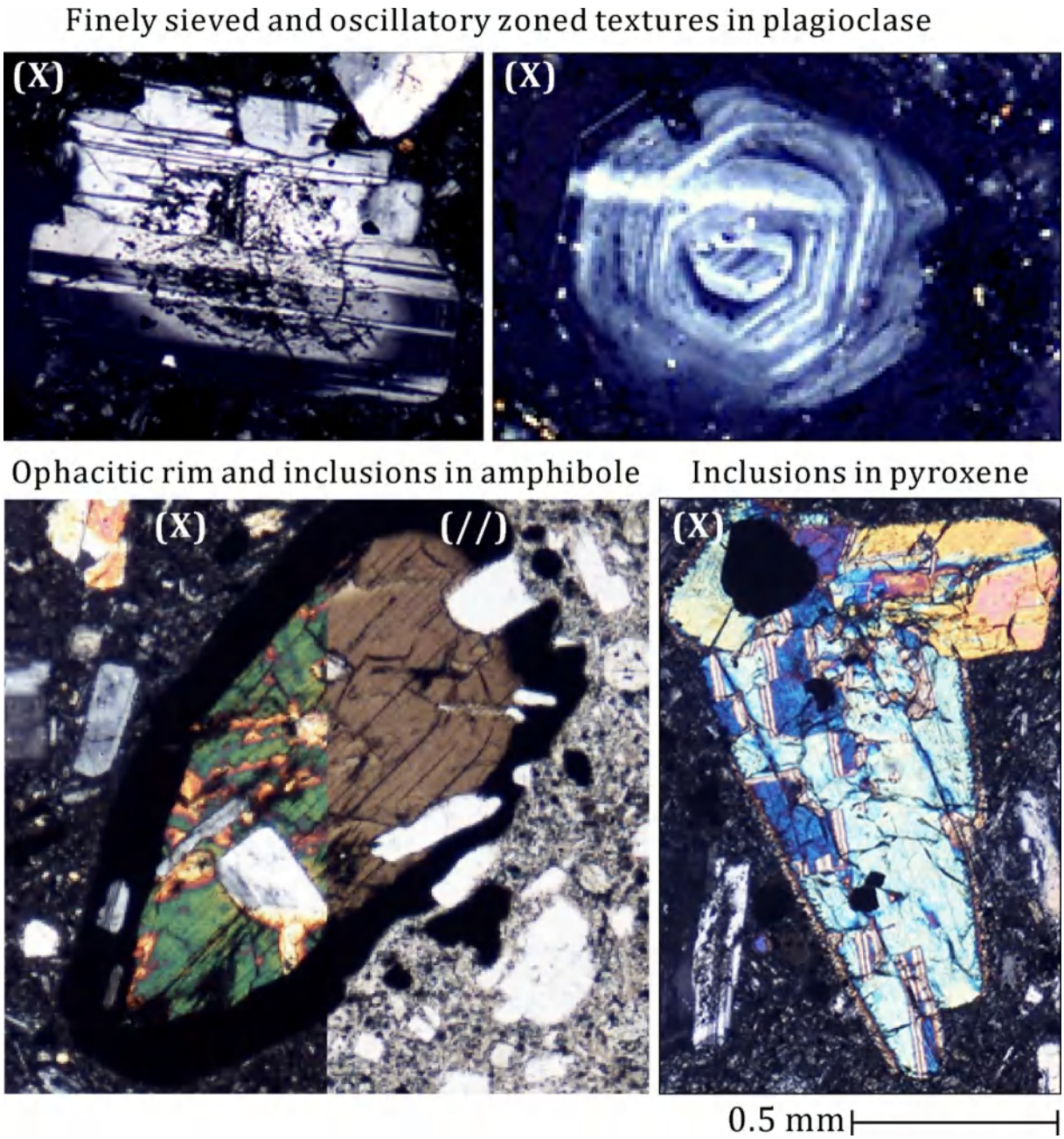

Fig. 5 Representative photomicrograph of finely sieved and oscillatory zoned textures in plagioclase phenocrysts (upper image), ophacitic rim texture in amphiboles, and mineral inclusions in both amphibole and pyroxene phenocrysts (lower image). (X) and (//) symbols represent cross- and plane-polarized images, respectively

magma types are enriched in Th and poor in Nb and Zr denies the possibility of crustal melting because this geochemical signature is typical for calc-alkaline subduction magmatism (e.g., Wood 1980; Demoux et al. 2009) (Fig. 6e). This idea is supported by the discovery of basaltic lithic clasts in old pyroclastic products by Sitorus et al. (1994), i.e., basalt was erupted during the relatively old phase of Mt. Sumbing, but was later buried by the younger products. Thus, we pointed out that the discussion of the geochemical relationship between the evolved and primitive samples will be crucial to advance the understanding of magma petrogenesis at Mt. Sumbing.

In addition, despite the significantly close distance between Mt. Sumbing and Mt. Sindoro (i.e., the two eruptive vents are only ~12 km from each other; Fig. 1b), we confirmed that both volcanoes do not share similar

Table 1 Summary of petrography and crystal size distribution (CSD) analysis of the studied samples. Oscillatory zoned, OZ; finely sieved, FS; non-zoned, NZ; ophacitic, Op

Sam-ple	Coordinate	Phases	Modal, vol%	Phenocryst fraction (ϕ_{PC})	Average phenocryst size (mm)	Textures	CSD slope (–)	Goodness of fit (Q)	Number of plagioclases used for CSD	R^2
LF1	– 7.315215 110.074101	Pl Px Amp Ox	80.5 9.2 4.7 5.6	0.44	0.25	FS, OZ, NZ NZ Op NZ	3.0	0.874	140	0.82
PDC1	– 7.327282, 110.048725	Pl Px Amp Opq	66.0 29.8 0.9 3.3	0.30	0.21	FS, OZ, NZ NZ NZ NZ	3.9	0.179	80	0.81
LF2	– 7.367248, 110.051117	Pl Px Amp Ox	77.4 16.6 3.3 2.7	0.31	0.23	FS, OZ, NZ NZ Op NZ	3.7	0.261	121	0.82
LF3	– 7.380006, 110.070307	Pl Px Amp Ox	65.1 25.5 2.0 7.4	0.48	0.25	FS, OZ, NZ NZ Op NZ	2.9	0.003	398	0.86
LF4	– 7.380285, 110.070855	Pl Px Amp Ox	80.0 10.2 3.4 6.4	0.32	0.22	FS, OZ, NZ NZ Op NZ	3.8	0.046	265	0.86
LF5	– 7.379715, 110.068904	Pl Px Amp Ox	77.0 8.9 7.8 6.3	0.41	0.18	FS, OZ, NZ NZ Op NZ	3.3	0.032	300	0.89
LF6	– 7.381545, 110.070986	Pl Px Amp Ox	74.8 15.2 2.0 8.0	0.25	0.18	FS, OZ, NZ NZ Op NZ	5.0	0.412	112	0.82
LF7	– 7.380260, 110.071284	Pl Px Amp Ox	75.3 11.7 5.2 7.8	0.38	0.19	FS, OZ, NZ NZ Op NZ	4.1	0.905	171	0.82
LD1	– 7.382504, 110.072491	Pl Px Amp Ox	69.7 0.3 29.7 0.3	0.42	0.23	OZ, FS, NZ NZ Op NZ	1.7	0.262	104	0.81
LD2	– 7.380959, 110.073506	Pl Px Amp Ox	70.1 0.4 25.0 4.5	0.45	0.25	OZ, FS, NZ NZ Op NZ	1.2	0.037	100	0.81

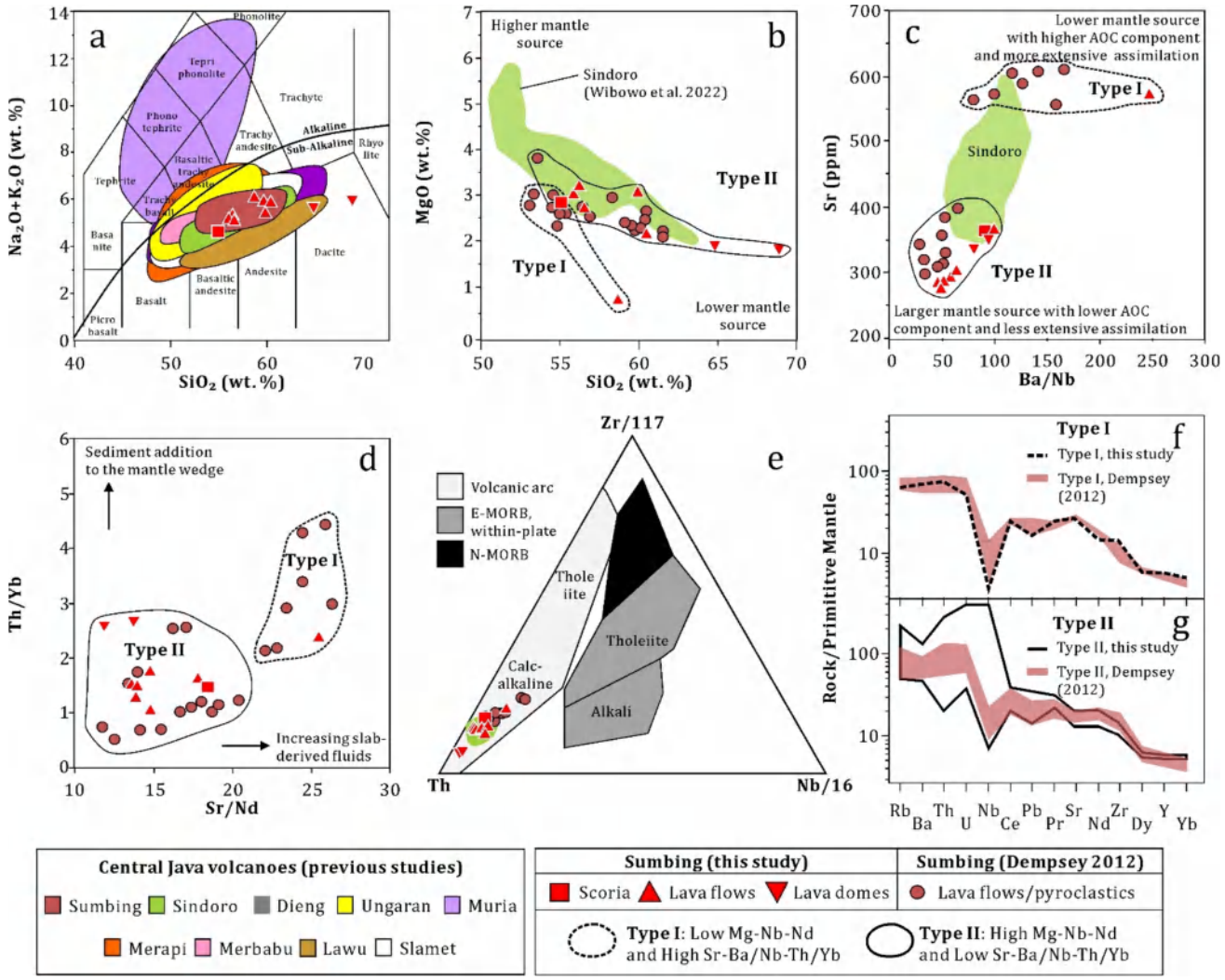

Fig. 6 **a** Plot of silica against alkalis shows that our samples (shown as red square and triangles) are classified as sub-alkalic basaltic andesite to dacite. Noteworthy, the LD2 sample is presently marked as the most silicic volcanic rock among all Quaternary volcanoes in Central Java (Merapi: Gertisser et al. 2023; Handley et al. 2011; Merbabu: Mulyaningsih and Shaban 2020; Lawu: Hartono 1994; Slamet: Harijoko et al. 2021; Sumbing: Dempsey 2013; Sindoro: Wibowo et al. 2022; Dieng: Harijoko et al. 2016; Ungaran: Suhendro et al. 2023a; Muria: Setidjadji et al. 2006). **b**, **c**, **d** Plot of SiO_2 against MgO, Ba/Nb against Sr, and Th/Yb against Sr/Nd shows the occurrence of two rock types, i.e., type I and II. Type I is typically poor in magnesium and niobium but rich in barium, strontium, and thorium. Conversely, type II has abundant magnesium, calcium, and niobium and is poor in barium, strontium, and thorium. **d** Zr–Th–Nb ternary plot (Wood et al. 1980) for the Sumbing and Sindoro samples. All samples are plotted in the calc-alkaline volcanic arc field. **f**, **g** Spider-diagrams of type I and II rocks. Note that Mt. Sumbing has different geochemical characteristics to Mt. Sindoro, implying that both volcanoes do not share a similar magmatic system

magma reservoirs because of the distinct geochemical characteristics (Fig. 6). The products of Mt. Sindoro are typically more enriched in magnesium and calcium than Mt. Sumbing (Fig. 6 and Table 2), suggesting a higher influx from the mantle source. One possible reason is that the slab depth beneath Mt. Sindoro is deeper than that of Mt. Sumbing (~220 and 200 km, respectively; Hayes et al. 2018).

5.2 Dynamics of the presently active type II magma

From stratigraphy, we can determine that the latest activity (from PDC1 towards the 1730 CE lava domes, i.e., LD2) of Mt. Sumbing is dominated by the extrusion of type II magma (Fig. 2). Thus, investigating the petrological (mineralogy and CSD) and geochemical data of type II in chronological

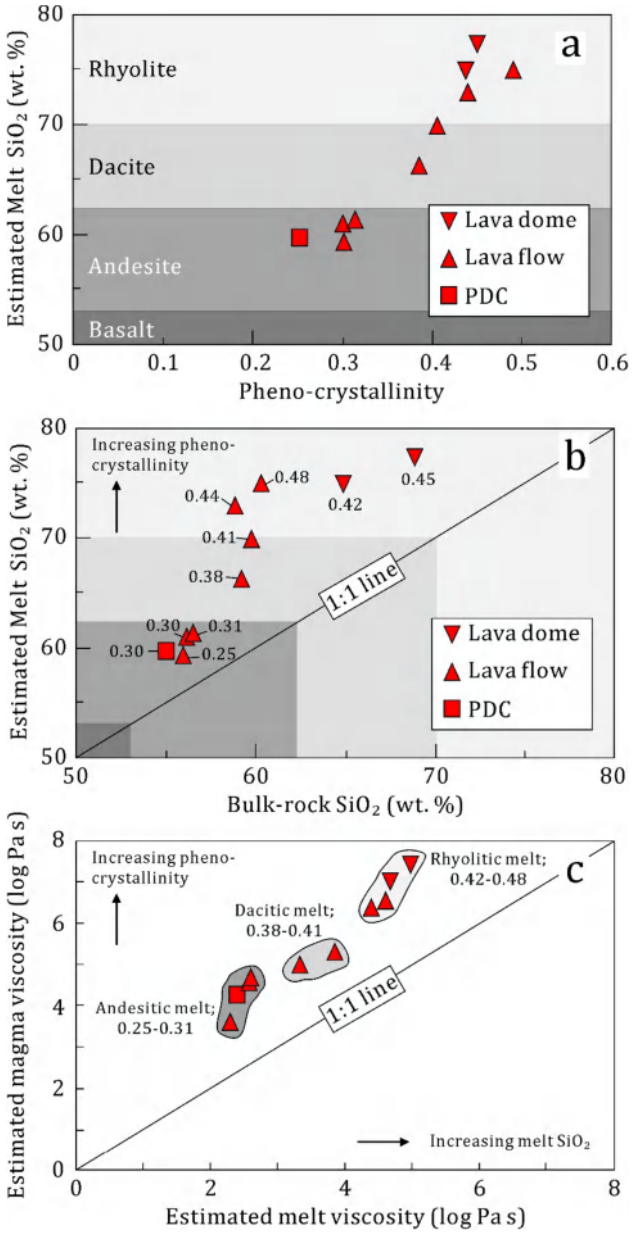

Fig. 7 **a**, **b** Bivariate plot between pheno-crystallinity and bulk-rock silica with estimated silica content in the melt. **c** Bivariate plot between the estimated melt viscosity and effective viscosity (phenocryst-included). Note that silica content in the melt and effective viscosity strongly depend on the crystallization intensity. Numbers in **b** and **c** denotes the pheno-crystallinity

order (i.e., stratigraphy) magma provides crucial information on the dynamics and temporal evolution of the presently active magma reservoir beneath Mt. Sumbing.

Under an equilibrium differentiation, the silica and phenocryst contents in magma periodically increase as a result of the more significant crystal nucleation and growth (Higgins 2002). This means that crystallization-fractionation is a time-dependent process, where a longer cooling history (or magma residence time) is often represented by a gentle CSD slope and vice versa (Higgins 2002). Such increasing silica content (bulk-rock and melt compositions) is also crucial for allowing the crystallization of more felsic and/or hydrous crystals, such as quartz and amphibole/biotite; in other words, magma avoids the crystallization of mafic minerals such as pyroxene, oxides, and olivine (McBirney 2007). While under disequilibrium differentiation, the silica content (bulk-rock and melt compositions) in magma decreases because of the injection of a hotter-less evolved magma. As silica content decreases (and temperature increase) the crystallization of mafic minerals becomes intense again, and causes the formation of finely sieved and reversely zoned textures (especially for plagioclase crystals; Renjith 2014, Gunawan and Suhendro 2023, Suhendro et al. 2023b). In addition, the mixing of two different crystal populations from different reservoirs is generally depicted by a kinking (i.e., non-linear) CSD slope (see Fig. 3.18 in Higgins 2002). At this condition, the CSD slope may be steepened because of the decreasing cooling time needed for crystal growth (Yamashita and Toramaru 2021).

We observed that pheno-crystallinity yielded a positive correlation with silica content (bulk-rock and melt compositions; see also Fig. 11b in Suhendro et al. 2023b) and resulted in a negative correlation with CSD slope from PDC1 to LF3 (Fig. 9). Such increasing silica and phenocryst contents were accompanied by the relative decrease of pyroxene and oxides (Fig. 4). This signature suggests that the early stage of type II magma underwent closed magma system with a predominantly equilibrium differentiation condition (Fig. 8). However, silica and phenocryst content were observed to fluctuate during the middle stage (from LF4 to LF6) and the CSD kink exclusively observed in LF4 and LF6 samples (Figs. 4, 9), implying that the magma alternatingly underwent equilibrium and disequilibrium differentiation conditions. This process can occur under open system magma reservoirs, facilitating some episodic mafic magma influx into the cooling magma reservoir (e.g., Blake 1981). It became more evident as finely sieved textures were typically rich in LF4, LF5, and LF6 samples. We suggest that type II magma shifted into a closed system again during the final stage (LF7 to LD2) due to the progressively increasing silica and phenocryst content and decreasing CSD slope and mafic mineral contents with time (Figs. 4, 9). However, the late stage of type II likely underwent a more closed system than the early stage because the magma has reached dacitic bulk-rock composition (up to 68.9 wt% SiO_2^{Bulk}) and rhyolitic melt composition (77.1 wt% SiO_2^{Melt}). The fact that LF7, LD1, and LD2 samples lacked finely sieved textures also does not deny this idea. In addition, the reason why LD samples preserve the most abundant oscillatory zoning texture is because they record the longest and the latest cooling

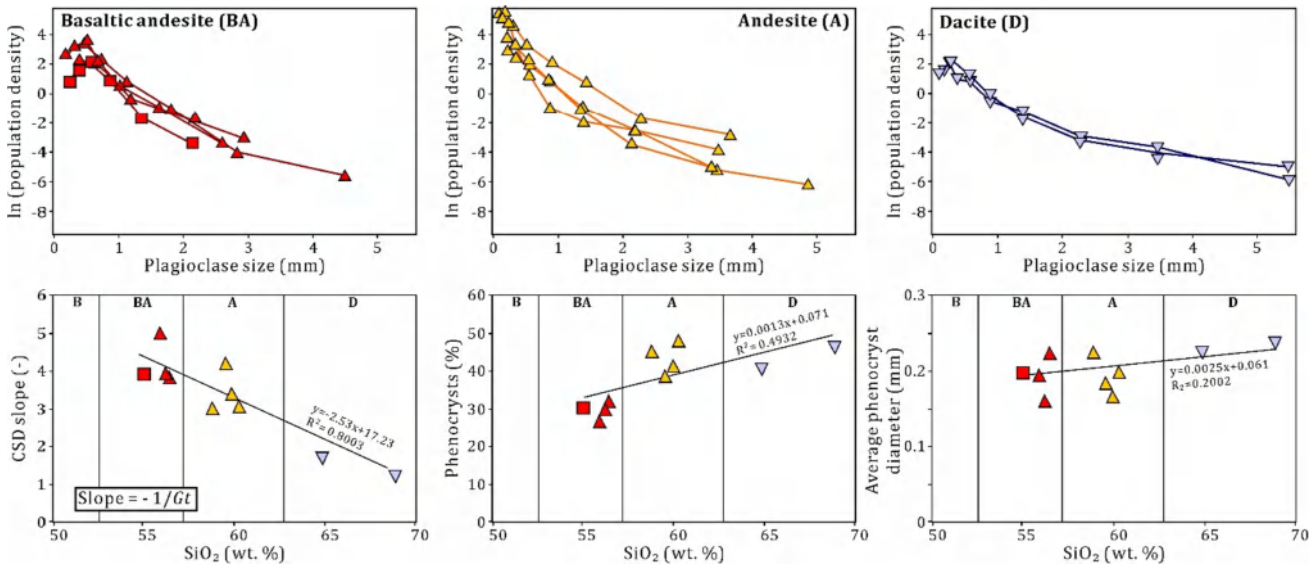

Fig. 8 Plagioclase size distribution (CSD) of basaltic andesite, andesite, and dacite samples of this study. Note that silica is negatively correlated with the CSD slope but yields a positive correlation with pheno-crystallinity and average phenocryst size

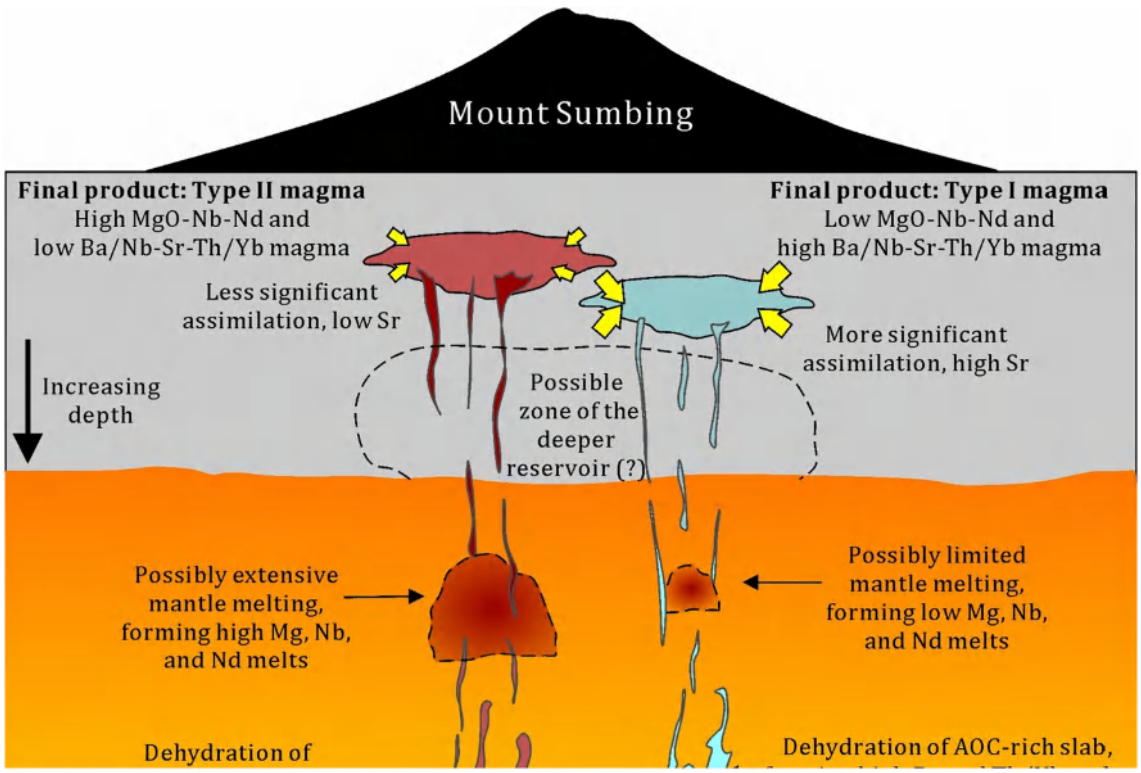

Fig. 9 Petrogenesis model of type I and type II magma beneath Mt. Sumbing. Blue colour on the subducted slab represents altered oceanic crust (AOC) material. Yellow arrow corresponds to crustal assimilation; larger crustal assimilation intensity is represented by large arrow and vice versa. Accumulation AOC-rich and mantle-poor melts that underwent significant crustal assimilation forms type I magma. While AOC-poor and mantle-rich melts which experienced less significant crustal assimilation yields type II magma

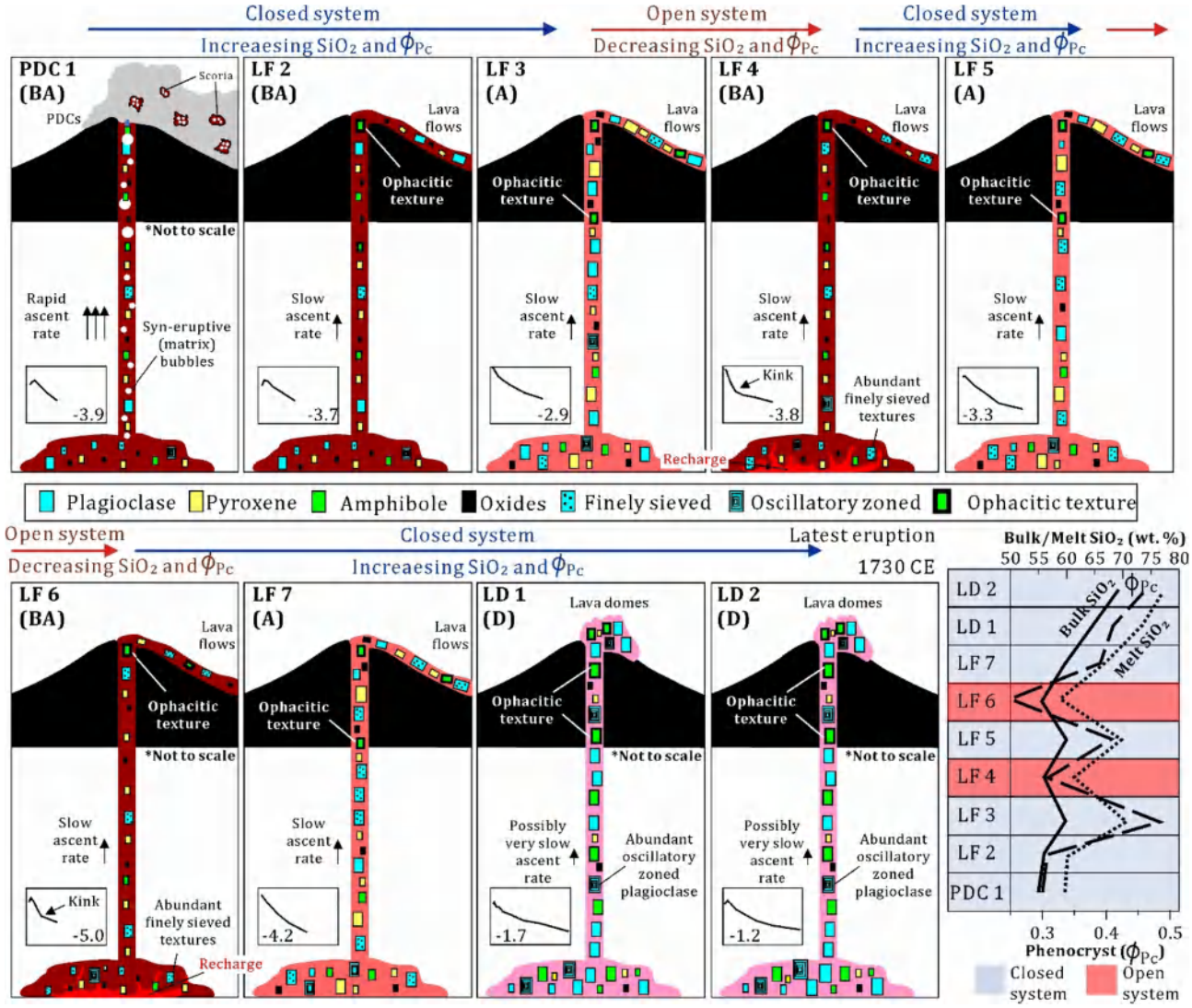

Fig. 10 Temporal dynamics of the presently active type II magma. Darker magma colour represents more mafic composition and vice versa. BA, A, and D is basaltic andesite, andesite, and dacite, respectively. Boxes within each panel represent the respective CSD curve for each sample. The solid and dashed line in the lower-right image corresponds to silica and phenocryst contents. The early stage of type II magma (PDC1–LF3) was considered a closed system, as indicated by the maturation of basaltic andesite into andesite magma with a progressively increasing phenocryst content and decreasing CSD slope. The evidence of fluctuating silica and phenocryst contents coupled with the occurrence of kinked and steep CSD curves strongly suggest the interchanging condition between open and closed magmatic systems during the middle stage (LF4–LF6). Finally, type II magma likely underwent a closed system again during the final stage (LF7–LD2) because the magma was able to reach dacitic composition (with a typically high phenocryst fraction and gentle CSD slope)

process. Noteworthy, the LD2 sample is presently marked as the most silicic volcanic rock among all Quaternary volcanoes in Central Java (Fig. 6a).

5.3 Possible hazard: insights from the physio-chemical magma conditions

Silica and magma decompression rates are believed as two of the most important factors that control volcanic eruption styles because they can significantly control magma viscosity and the extent of syn-eruptive bubble nucleation (Sigurdsson 2000; Takeuchi 2011; Toramaru 2006, 2014; Shea 2017). Under a slow magma decompression rate (< 0.001 MPa/s), low-viscosity magmas ($< 10^5$ Pa s) tend to produce lava flows, whereas high-viscosity magmas ($> 10^5$ Pa s) form lava domes (Cassidy et al. 2018; Starodubtsev et al. 2023; Suhendro et al. 2023a)). In such an effusive manner, amphibole crystals are often rimmed by breakdown texture due to slow dehydration during magma ascent (e.g., Gertisser et al. 2011). The fact that most amphibole crystals in our lava samples displayed breakdown texture supports the idea of slow magma ascent (Fig. 10). While under a high magma

Table 2 Whole-rock XRF results of the studied samples. LF, LD, and PDC denote lava flow, lava dome, and scoria-pyroclastic density current, respectively. All samples were fresh (LOI varied from 0.1 to 1%) and normalized to 100 wt% (volatile-free)

	LF1 Type I	PDC1 Type II	LF2 Type II	LF3 Type II	LF4 Type II	LF5 Type II	LF6 Type II	LF7 Type II	LD1 Type II	LD2 Type II
SiO_2 (wt%)	58.74	55.04	56.21	60.25	56.45	59.72	55.88	59.52	64.82	68.90
TiO_2 (wt%)	0.71	0.97	0.97	0.83	0.95	0.62	0.96	0.83	0.46	0.51
Al_2O_3 (wt%)	17.89	18.04	17.13	16.80	17.61	16.47	17.42	17.23	15.73	13.89
MnO (wt%)	0.17	0.17	0.17	0.15	0.16	0.14	0.16	0.15	0.12	0.11
MgO (wt%)	0.84	3.18	3.34	2.27	2.82	3.18	3.10	2.42	2.07	1.99
CaO (wt%)	4.43	6.71	7.56	6.00	6.88	6.70	7.18	6.25	4.79	3.63
Na_2O (wt%)	3.15	3.07	3.78	3.88	3.53	3.44	3.61	3.85	3.34	3.45
K_2O (wt%)	2.88	1.52	1.61	1.94	1.58	1.94	1.54	1.90	2.37	2.35
P_2O_5 (wt%)	0.28	0.21	0.18	0.18	0.19	0.16	0.19	0.18	0.18	0.06
Fe_2O_3 (wt%)	7.75	8.74	5.38	7.55	8.18	6.93	8.54	7.54	4.85	3.37
Total (wt%)	100.00	100.00	100.00	100.00	100.00	100.00	100.00	100.00	100.00	100.00
Ba (ppm)	669.30	488.80	345.50	407.20	379.00	476.40	348.80	407.20	640.60	709.40
Ce (ppm)	49.90	41.70	36.10	42.70	42.50	44.30	38.40	42.70	63.50	66.80
Co (ppm)	31.00	45.80	45.30	46.90	41.60	43.90	43.90	46.90	26.60	30.20
Cr (ppm)	n.d	n.d	n.d	n.d	n.d	n.d	n.d	n.d	n.d	n.d
Cu (ppm)	45.00	22.50	15.30	10.10	13.10	29.10	15.20	10.10	13.70	12.00
Dy (ppm)	4.00	4.00	4.01	3.96	3.98	3.94	4.00	3.96	3.86	3.84
Ga (ppm)	19.10	18.60	18.20	18.70	18.50	18.70	18.40	18.70	19.80	20.20
Hf (ppm)	4.56	4.50	3.62	4.71	4.39	4.33	3.68	4.71	4.21	5.33
Mo (ppm)	n.d	n.d	n.d	n.d	n.d	n.d	n.d	n.d	n.d	n.d
Nb (ppm)	2.72	4.83	7.23	7.04	7.49	4.65	7.22	7.04	6.93	8.52
Nd (ppm)	22.70	20.10	18.50	20.60	20.40	21.20	19.20	20.60	26.90	28.00
Ni (ppm)	1.33	10.48	n.d	1.23	n.d	2.99	n.d	1.23	8.30	5.06
Pb (ppm)	11.76	11.52	10.08	12.20	10.91	12.79	10.45	12.20	23.41	19.73
Pr (ppm)	6.99	6.38	6.00	6.44	6.40	6.59	6.13	6.44	8.04	8.19
Rb (ppm)	69.00	39.20	32.50	43.70	33.60	51.10	32.00	43.70	71.90	81.00
Sc (ppm)	17.36	23.59	24.54	18.23	23.19	17.03	23.30	18.23	8.97	8.01
Sr (ppm)	574.40	368.20	272.60	281.20	283.90	377.40	282.80	281.20	368.50	332.90
Th (ppm)	10.78	6.22	1.76	7.62	5.35	8.17	4.04	7.62	17.10	20.48
U (ppm)	2.39	1.08	0.77	1.31	0.86	1.65	0.78	1.31	2.52	2.96
V (ppm)	161.60	200.00	206.40	162.80	199.90	122.60	197.80	162.80	75.70	82.30
Y (ppm)	23.8	23.80	20.60	21.00	24.40	19.20	21.20	21.00	21.50	22.90
Yb (ppm)	4.56	4.31	3.79	5.05	4.22	5.06	4.07	5.05	6.42	7.86
Zn (ppm)	77.90	85.90	80.40	92.20	96.60	73.80	82.80	92.20	64.10	60.90
Zr (ppm)	137.10	158.60	119.80	141.80	132.20	149.80	128.20	141.80	149.90	170.30

decompression rate (> 0.001 MPa/s), both low and high-viscosity magmas may form explosive eruptions, forming either buoyant eruption plumes and/or extensive PDCs (e.g., Toramaru 2006; Cassidy et al. 2018). In this rapid magma ascent condition, amphibole crystals are typically fine and avoid breakdown texture, such as in our scoria-PDC1 sample (Fig. 10).

Using the phenocryst-extraction method to estimate the silica composition in glass and equations from Murase et al. (1985), and Takeuchi (2015), we roughly estimate that the studied samples had magma viscosity ranging from $10^{3.6}$ to $10^{7.5}$ Pa s, where the highest viscosity value represent the latest product of Mt. Sumbing (i.e., LD2) (Fig. 7c). This suggests that the presently active Mt. Sumbing magma has reached the high viscosity regime, and the viscosity might still increase if the equilibrium crystallization continues to occur and form rhyolitic magma. Under this condition, the future eruptions at Mt. Sumbing will likely be effusive dome-forming and/or plume-forming explosive eruptions, depending on the magma decompression rates. It should be noted that both styles are considerably hazardous. For instance, the presence of lava domes can stimulate the formation of explosive eruptions via gas accumulation in the conduit (e.g., Alfano et al. 2011; Surono et al. 2012; Maeno et al. 2019) and/or unpredictable PDCs via dome collapse, without any precursory sign (e.g., Shimizu 2022; Breard et al.

2023). While direct plume-forming eruptions may cause a real-time hazard and significant human disruption over large areas (e.g., Hayes et al. 2019; Williams et al. 2020).

In addition, many studies have shown that crystallization of amphibole phenocryst can occur at pressures ranging between 100 and 1000 MPa, as long as the magma is saturated with water (typically 4–6 wt%) and does not exceed 900 °C (e.g., Couch et al. 2001, 2003; Ridolfi and Renzulli 2012; Costa et al. 2013). Thus, the exceptionally high amphibole content in the latest products (i.e., lava domes; 25.0–29.6 vol%) compared to the other older samples (i.e., lava flow and scoria; <8 vol%) indicates that the presently active type II magma has been relatively cold (~824 °C for LD1 and 801 °C for LD2; Table 3) and supersaturated in magmatic water. Because a high magmatic water content may facilitate extensive nucleation of pheno-bubbles (i.e., pre-eruptive bubbles; Toramaru 2014; Suhendro et al. 2022), and the fraction of pheno-bubble is proportional to magma compressibility and eruption magnitude (Caricchi et al. 2014; Parmigiani et al. 2016), there is a possibility that Mt. Sumbing is currently building overpressure which is needed for triggering high-magnitude explosive eruptions. Therefore, we pointed out that investigations on the present volatile budget via petrological and geophysical methods are highly crucial to validate this issue, as well as for advancing the hazard-mitigation system at Mt. Sumbing.

6 Conclusion

This is the first study that recognized the occurrence of (at least) two magma reservoirs beneath Mt. Sumbing, namely type I and type II. Type I magma is likely derived from AOC-rich and mantle-poor melts, as indicated by the high Ba-Th, and low MgO–Nb–Nd values. By contrast, type II magma originates from AOC-poor and mantle-rich melts because of the low Ba-Th and high MgO–Nb–Nd values. Moreover, type I magma is characterized by significantly higher Sr contents than type II magma, suggesting a more extensive crustal assimilation process. From stratigraphy, we can determine that the latest activity of Mt. Sumbing is dominated by the extrusion of type II magma (i.e., the presently active magma reservoir). This magma was under closed system conditions during the early phase (PDC1, LF2, and LF3), causing the maturation of basaltic andesite magma into andesite magma with larger phenocryst size and gentler CSD slope. The silica and phenocryst content fluctuated during the following middle stage (LF4, LF5, and LF6); this signature suggests the interchanging conditions between open and closed systems. This idea is supported by the fact that LF4 and LF6 samples showed abundant finely-sieved textures and steep-kinked CSD curves. Finally, type II magma shifted into a closed system again during the final stage (LF7, LD1, and LD2) because the CSD slope decreased, and the silica and phenocryst contents progressively increased with time, forming dacites. Under this presently silicic (and viscous) magma composition, we pointed out that the future eruptions at Mt. Sumbing will likely be effusive dome-forming and/or plume-forming explosive eruptions, depending on the magma decompression rates.

Table 3 Estimated silica content in the melt, temperature, melt viscosity (phenocryst-free), and magma viscosity (phenocryst-included) of the studied rocks

Unit	Estimated SiO_2^{Melt} (wt%; from Eq. 3)	Estimated temperature (*K;* from Eq. 4)	Estimated melt viscosity (log Pa/ s; from Eq. 5)	Estimated magma viscosity (log Pa/ s; from Eq. 6)
LD2	77.1	1073.8	4.9	7.5
LD1	75.1	1097.6	4.6	6.9
LF7	66.1	1217.9	3.4	4.9
LF6	58.9	1333.8	2.3	3.6
LF5	69.6	1167.4	3.9	5.3
LF4	61.0	1297.1	2.5	4.7
LF3	74.8	1100.9	4.6	6.5
LF2	60.8	1301.9	2.5	4.5
PDC1	59.7	1320.2	2.4	4.2
LF1	72.5	1116.6	4.5	6.3

Acknowledgements This research was funded by the Faculty of Geography under the scheme of "Dana Hibah Penelitian Mandiri Dosen Tahun 2023 Tahap 1". We thank Dr. Agus-Budi Santoso, Dr. Hanik Humaida, Lestari Agustiningtyas, Niken Angga Rukmini, and Mas Dodo from the Balai Penyelidikan dan Pengembangan Teknologi Kebencanaan Geologi (BPPTKG) Yogyakarta for their support and guidance for XRF analysis. We also thank two anonymous reviewers for the constructive comments and the editor (Dr. Binbin Wang) for handling this manuscript. Dr. Haryo Edi Wibowo from the Department of Geological Engineering is also thanked for the fruitful discussions. Ibana Zuhru Wardiea is appreciated for her companion during the fieldwork.

Author contributions I.S. conceptualized the research, collected the funding, conducted fieldwork, supervised all analyses, interpreted the data, data curation, and wrote the manuscript. E.Y., R.F.Z., P.E.P., Z.Y.R., S.D., M.AT.S.P.S., A.J., and G.A.E.Z.L. joined the fieldwork, and conducted all analyses. All authors contributed to refining the manuscript.

Declarations

Competing interests The authors declare that they have no known competing financial interests or personal relationships that could have appeared to influence the work reported in this paper.

References

Alfano F, Bonadonna C, Volentik ACM, Connor CB, Watt SFL, Pyle DM, Connor LJ (2011) Tephra stratigraphy and eruptive volume of the May, 2008, Chaitén eruption, Chile. Bull Volcanol. 73:613–630. https://doi.org/10.1007/s00445-010-0428-x

Blake S (1981) Volcanism and the dynamics of open magma chambers. Nature. 289:783–785. https://doi.org/10.1038/289783a0

Bohm M, Haberland C, Asch G (2013) Tectonophysics imaging fluid-related subduction processes beneath Central Java (Indonesia) using seismic attenuation tomography. Tectonophysics. 590:175–188. https://doi.org/10.1016/j.tecto.2013.01.021

Breard ECP, Dufek J, Chabonnier S, Gueugneau V, Giachetti T, Walsh B (2023) The fragmentation-induced fluidization of pyroclastic density currents. Nat Commun. 14:2079. https://doi.org/10.1038/s41467-023-37867-1

Caricchi L, Annen C, Blundy J, Simpson G, Pinel V (2014) Frequency and magnitude of volcanic eruptions controlled by magma injection and buoyancy. Nat Geosci. 7:126–130.

Cassidy M, Manga M, Cashman K, Bachmann O (2018) Controls on explosive-effusive volcanic eruption styles. Nat Commun. 9:2839. https://doi.org/10.1038/s41467-018-05293-3

Costa F, Andreastuti S, Bouvet de Maisonneuve C, Pallister JS (2013) Petrological insights into the storage conditions, and magmatic processes that yielded the centennial 2010 Merapi explosive eruption. J Volcanol Geotherm Res. 261:209–235. https://doi.org/10.1016/j.jvolgeores.2012.12.025

Couch S, Sparks RSJ, Carroll MR (2001) Mineral disequilibrium in lavas explained by convective self-mixing in open magma chambers. Nature. 44:1037–1039.

Couch S, Harford CL, Sparks RSJ, Carroll MR (2003) Experimental constraints on the conditions of formation of highly calcic plagioclase microlites at the Soufrière Hills volcano, Montserrat. J Petrol. 44:1455–1475.

Davidson JP (1987) Crustal contamination versus subduction zone enrichment: examples from the Lesser Antilles and implications for the mantle source composition of island arc volcanic rocks. Geochim Cosmochim Acta. 51:2185–2198.

De Astis G, Peccerillo A, Kempton PD, La Volpe L, Wu TW (2000) Transition from calc-alkaline to potassium-rich magmatism in subduction environments: geochemical and Sr, Nd, Pb isotopic constraints from the island of Vulcano (Aeolian arc). Contrib Miner Petrol. 139:684–703.

Demoux A, Kroner A, Hegne E, Badarch G (2009) Devonian arc-related magmatism in the Tseel terrane of SW Mongolia: chronological and geochemical evidence. J Geol Soc. 166:1–13. https://doi.org/10.1144/0016-76492008-090

Dempsey SR (2013) Geochemistry of volcanic rocks from the Sunda Arc. Dissertation, Durham University.

Elliot T, Plank T, Zindler A, White WM, Bourdon B (1997) Element transport from the slab to volcanic front at the Mariana arc. J Geophys Res. 102:14991–15019.

Forni F, Bachmann O, Mollo S, De Astis G, Gelman SE, Ellis BS (2016) The origin of a zoned ignimbrite: insights into the Campanian Ignimbrite magma chamber (Campi Flegrei, Italy). Earth Planet Sci Lett. 449:259–271. https://doi.org/10.1016/j.epsl.2016.06.003

Gertisser R, Charbonnier SJ, Troll VR, Keller J, Preece K, Chadwick JP, Barclay J, Herd RA (2011) Merapi (Java Indonesia): Anatomy of a killer volcano. Geology Today. 27(2) 57–62. https://doi.org/10.1111/gto.2011.27.issue-2 https://doi.org/10.1111/j.1365-2451.2011.00786.x

Gertisser R, Charbonnier SJ, Keller J, Quidelleur X (2012) The geological evolution of Merapi volcano, Central Java, Indonesia. Bull Volcanol. 74:1213–1233. https://doi.org/10.1007/s00445-012-0591-3

Gertisser R, Troll VR, Walter TR, Nandaka IGMA, Ratdomopurbo A (2023) Merapi volcano: geology, eruptive activity, and monitoring of a high-risk volcano. Springer, Cham. https://doi.org/10.1007/978-3-031-15040-1

Ginibre C, Wörner G, Krornz A (2004) Structure and dynamics of the Laacher See Magma Chamber (Eifel, Germany) from major and trace element zoning in sanidine: a cathodoluminescence and electron microprobe study. J Petrol. 45(11):2197–2223. https://doi.org/10.1093/petrology/egh053

Gunawan RMPP, Suhendro I (2023) Chemical and textual studies of the youngest pyroclastic deposits at Mt. Seminung (Souh Sumatra, Indonesia): A window for understanding the explosive behavior of a post-caldera volcano. Rudarsko-Geološko-Naftni Zbornik. 38(5):61–77. https://doi.org/10.17794/rgn.2023.5.6

Handley HK, Macpherson CG, Davidson JP, Berlo K, Lowry D (2007) Constraining fluid and sediment contributions to subduction-related magmatism in Indonesia: Ijen volcanic complex. J Petrol. 48(6):1155–1183. https://doi.org/10.1093/petrology/egm013

Handley HK, Turner S, Macpherson CG, Gertisser R, Davidson JP (2011) Hf-Nd isotope and trace element constraints on subduction inputs at island arcs: limitations of Hf anomalies as sediment input indicators. Earth Planet Sci Lett. 304:212–223.

Harijoko A, Uruma R, Wibowo HE, Setijadji LD, Imai A, Yonezu K, Watanabe K (2016) Geochronology and magmatic evolution of the Dieng Volcanic Complex, Central Java, Indonesia and their relationships to geothermal resources. J Volcanol Geotherm Res. 310:209–224. https://doi.org/10.1016/j.jvolgeores.2015.12.010

Harijoko A, Sari SA, Wibowo HE, Setiawan NI, Moktikanana MLA (2021) Stratigraphy, chronology, and magma evolution of Holocene volcanic products from Mt. Slamet deposited in the Guci Valley, Central Java, Indonesia. J Volcanol Geotherm Res. 418:107341.

Hartono U (1994) The petrology and geochemistry of the Willis and Lawu volcanoes, East Java, Indonesia. Dissertation, University of Tasmania.

Hayes JL, Deligne NI, Bertin L, Calderon R, Wardman JB, Wilson TM, Leonard GS, Stewart C, Wallace KL, Baxter PJ (2019) Impacts of the 2015 eruption of Calbuco volcano on Chilean infrastructure, utilities, agriculture, and health. Lower Hutt (NZ): GNS science report.

Higgins MD (2002) Quantitative textural measurements in igneous and metamorphic petrology. Cambridge University Press.

Kaneko K, Kamata H, Koyaguchi T, Yoshikawa M, Furukawa K (2007) Repeated large-scale eruptions from a single compositionally stratified magma chamber: An example from Aso volcano, Southwest Japan. J Volcanol Geoth Res. 167:160–180. https://doi.org/10.1016/j.jvolgeores.2007.05.002

Maeno F, Nakada S, Yoshimoto M, Shimano T, Hokanishi N, Zaennudin A, Iguchi M (2019) A sequence of a plinian eruption preceded by dome destruction at Kelud volcano, Indonesia, on February 13, 2014, revealed from tephra fallout and pyroclastic density current deposits. J Volcanol Geotherm Res. 382:24–41. https://doi.org/10.1016/j.jvolgeores.2017.03.002

McBirney AR (2007) Igneous petrology, 3rd edn. Jones and Bartlett, Burlington.

Mitsuoka T, Toramaru A, Harijoko A, Wibowo HE (2021) Eruption types and conduit dynamics of Kukusan and Genteng volcanoes of the Ijen volcanic complex, Indonesia. Kyushu Univ Int Reposit Ser D Earth Planet Sci. 35:1–17

Morgan DJ, Jerram DA (2006) On estimating crystal shape for crystal size distribution analysis. J Volcanol Geotherm Res 154(1-2):1–7. https://doi.org/10.1016/j.jvolgeores.2005.09.016

Mulyaningsih S, Shaban G (2020) Geochemistry of Basaltic Merbabu Volcanic Rocks, Central Java, Indonesia. Indonesian J Geosci 7(2). https://doi.org/10.17014/ijog.7.2.161-178

Münker C, Wörner G, Yogodzinski G, Churikova T (2004) Behaviour of high field strength elements in subduction zones: constraints from Kamchatka-Aleutian arc lavas. Earth Planet Sci Lett. 224(3–4):285–293. https://doi.org/10.1016/j.epsl.2004.05.030

Murase T, McBirney AR, Melson WG (1985) Viscosity of the dome of Mount St. Helens. J Volcanol Geotherm Res. 24:193–204.

Parmigiani A, Faroughi S, Huber C, Bachmann O, Su Y (2016) Bubble accumulation and its role in the evolution of magma reservoirs in the upper crust. Nature. 532:492–495. https://doi.org/10.1038/nature17401

Pearce JA, Sternr RJ, Bloomer SH, Fryer P (2005) Geochemical mapping of the Mariana arc-basin system: implications for the nature and distribution of subduction components. Geochem Geophys Geosyst. 6:Q07006. https://doi.org/10.1007/s00410-011-0704-6

Prambada O, Arakawa Y, Ikehata K, Furukawa R, Takada A, Wibowo HE, Nakagawa M, Kartadinata MN (2016) Eruptive history of Sundoro volcano, Central Java, Indonesia. Bull Volcanol. 78:81. https://doi.org/10.1007/s00445-016-1079-3

Renjith ML (2014) Micro-textures in plagioclase from 1994–1995 eruption, Barren Island Volcano: evidence of dynamic magma plumbing system in the Andaman subduction zone. Geosci Front. 5:113–126. https://doi.org/10.1016/j.gsf.2013.03.006

Ridolfi F, Renzulli A (2012) Calcic amphiboles in calc-alkaline and alkaline magmas: thermobarometric and chemometric empirical equations valid up to 1,130°C and 2.2 GPa. Contrib Miner Petrol. 163:877–895. https://doi.org/10.1007/s00410-011-0704-6

Setidjadji LD, Kajino S, Imai A, Watanabe K (2006) Cenozoic island arc magmatism in Java Island (Sunda Arc, Indonesia): clues on relationships between geodynamics of volcanic centers and ore mineralization. Resour Geol. 56(3):267–292.

Shea T (2017) Bubble nucleation in magmas: a dominantly heterogeneous process? J Volcanol Geotherm Res. 343:155–170. https://doi.org/10.1016/j.jvolgeores.2017.06.025

Shimizu HA (2022) Numerical simulations of dome-collapse pyroclastic density currents using faSavageHutterFOAM: application to the 3 June 1991 eruption of Unzen volcano, Japan. J Disaster Res. 17:768–778. https://doi.org/10.20965/jdr.2022.p0768

Sigurdsson H (2000) Encyclopedia of volcanoes. Academic Press.

Sitorus K, Erfan RD, Bacharudin R, Mulyana AR (1994) Geological map of Sumbing volcano, Central Java. Volcanological Survey of Indonesia.

Starodubtsev IS, Starodubtseva YV, Tsepelev IA, Ismail-Zadeh AT (2023) Three-dimensional numerical modedlling gof lava dynamics using the smoothed particle hydrodynamics method. J Volcanol Seismol. 17(3):175–186. https://doi.org/10.1134/S0742046323700185

Straub SM, Gómez-Tuena A, Vannuchi P (2020) Subduction erosion and arc volcanism. Nat Rev. 1:574–589. https://doi.org/10.1038/s43017-020-0095-1

Suhendro I, Toramaru A, Harijoko A, Wibowo HE (2022) The origins of transparent and non-transparent white pumice: a case study of the 52 ka Maninjau caldera-forming eruption, Indonesia. J Volcanol Geotherm Res. https://doi.org/10.1016/j.jvolgeores.2022.107643

Suhendro I, Al Aro AS, Palembang MF, Rahim AP, Sari LR (2023a) On the formation of lava flows and lava domes in mafic-intermediate magmas (Mount Ungaran, Central Java, Indonesia). J Volcanol Seismol 17(3):228–245. https://doi.org/10.1134/S0742046323700148

Suhendro I, Naen GNRB, Gurusinga A, Sari SA, Moktikanana MLA, Gunawan RMPP, Jane J, Qodri MF, Sya'bana F, Cahyani SM, Ardian DN (2023b) Dynamics of the Young Merapi (<2.2 ka – 1788 CE) pumice fall deposits: Insights from textural and geochemical studies. J Volcanol Geotherm Res 443:107–919. https://doi.org/10.1016/j.jvolgeores.2023.107919

Surono A, Jousset P, Pallister J, Boichu M, Buongiorno MF, Budissantoso A, Costa F, Andreastuti S, Prata F, Schneider D, Clarisse K, Humaida H, Sumarti S, Bignami C, Griswold J, Carn S, Oppenheimer C, Lavigne F (2012) The 2010 explosive eruption of Java's Merapi volcano-A '100 year' event. J Volcanol Geotherm Res 241–242:121–135. https://doi.org/10.1016/j.jvolgeores.2012.06.018

Takeuchi S (2011) Preeruptivie magma viscosity: an important measure of magma eruptibility. J Geophys Res. https://doi.org/10.1029/2011JB008243

Takeuchi S (2015) A melt viscosity scale for preeruptive magmas. Bull Volcanol. 77:41. https://doi.org/10.1007/s00445-015-0929-8

Taverne NJM (1926) Vulkanstudien Op Java. Vulk Meded. 7:1–132.

Toramaru A (2006) BND (bubble number density) decompression rate meter for explosive volcanic eruptions. J Volcanol Geoth Res. 154:303–316. https://doi.org/10.1016/j.jvolgeores.2006.03.027

Toramaru A (2014) On the second nucleation of bubbles in magmas under sudden decompression. Earth Planet Sci Lett. 404:190–199. https://doi.org/10.1016/j.epsl.2014.07.035

Tregoning P, Brunner FK, Bock Y, Puntodewo SSO, McCaffrey R, Genrich JF, Calais E, Rais J, Subarya C (1994) First geodetic measurement of convergence across the Java Trench. Geophys Res Lett. 21(19):2135–2138.

Wibowo HE, Nakagawa M, Kuritani T, Furukawa R, Prambada O, Harijoko A (2022) Petological and geochemical study of Sundoro volcano, Central Java, Indonesia: temporal variations in differentiation and source processes during the growth of an individual volcano. J Petrol. 63:1–22. https://doi.org/10.1093/petrology/egac083

Wölbern I, Rumpker G (2016) Crustal thickness beneath Central and East Java (Indonesia) inferred from P receiver functions. J Asian Earth Sci. 115:69–79. https://doi.org/10.1016/j.jseaes.2015.09.001

Wood DA (1980) The application of a Th–Hf–Ta diagram to problems of tectomagmatic classification and to establishing the nature of crustal contamination of fbasaaltic lavas of the British Tertiary volcanic province. Earth Planet Sci Lett. 50:11–30.

Yamashita S, Toramaru A (2021) Control of magma plumbing systems on long-term eruptive behavior of Sakurajima volcano, Japan: insights from crystal-size-distribution analysis. In: Dynamic magma evolution, geophysical monograph. 254, 1st edn.